

pubs.acs.org/journal/apchd5 Article

# Efficient Topology-Optimized Couplers for On-Chip Single-Photon Sources

Omer Yesilyurt, <sup>§</sup> Zhaxylyk A. Kudyshev, <sup>§</sup> Alexandra Boltasseva, Vladimir M. Shalaev, and Alexander V. Kildishev\*



Cite This: ACS Photonics 2021, 8, 3061-3068



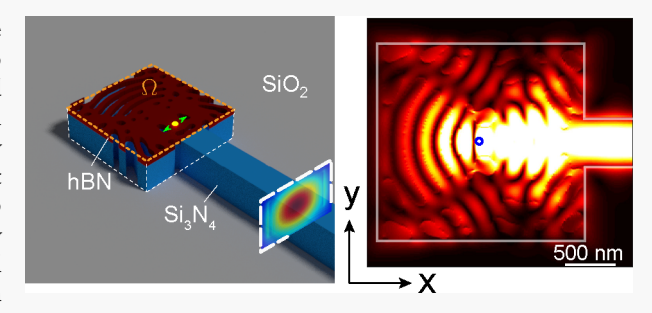
**ACCESS** 

III Metrics & More

Article Recommendations

Supporting Information

ABSTRACT: Room-temperature single-photon sources (SPSs) are critical for emerging practical quantum applications such as on-chip photonic circuity for quantum communications systems and integrated quantum sensors. However, the direct integration of an SPS into on-chip photonic systems remains challenging due to low coupling efficiencies between the SPS and the photonic circuitry that often involve size mismatch and dissimilar materials. Here we develop an adjoint topology optimization scheme to design high-efficiency couplers between a photonic waveguide and an SPS in hexagonal boron nitride (hBN). The algorithm accounts for fabrication constraints and SPS location uncertainty. First, a library of designs



for the different positions of the hBN flake containing an SPS with respect to a  $Si_3N_4$  waveguide is generated, demonstrating an average coupling efficiency of 78%. Then, the designs are inspected with a dimensionality reduction technique to investigate the relationship between the device geometry (topology) and the performance. The fundamental, physics-based intuition gained from this approach could enable the design of high-performance quantum devices.

KEYWORDS: single-photon emitter, on-chip, topology optimization

hotonics is a promising route to practical quantum information processing applications because it offers high speed, tolerance to decoherence in transparent environments, and high internal degrees of freedom, which can be used for quantum state encoding.1 Leveraging the recent advances in classical photonic integrated circuits, various elements of quantum photonic integrated circuits (QPICs)<sup>2-5</sup> have already been demonstrated at a proof-of-concept level. The realization of scalable QPICs is a critical milestone on the way to practical quantum photonic computing,6 quantum information processing applications, quantum communication,<sup>7,8</sup> quantum sensing,<sup>9</sup> quantum key distribution,<sup>10</sup> and machine learning.11 The operation of the QPICs consists of three main parts: (i) generation of predefined quantum states, (ii) transformation of the quantum states via linear and nonlinear on-chip photonic elements, and (iii) quantum state readout.<sup>12</sup> Although different components of the QPICs have been demonstrated, there is not yet a clear pathway for the practical realization of scalable QPICs, which requires the development of highly efficient, on-chip components for each of the parts of the QPIC. An essential aspect of the design of QPICs is compatibility with large-scale fabrication techniques, such as e-beam, photolithography, and etching, in terms of tolerance against the imperfections introduced during the fabrication process. Advanced optimization frameworks conventionally used to solve a broad range of design problems

in classical photonics could be employed to address the highly constrained optimization problem of QPIC design. There are two main paradigms for the integrated photonic component development: (i) methods based on prior knowledge or scientific intuition and (ii) algorithm-driven inverse design optimization frameworks. 13 The designs obtained with the first approach demonstrate simplified geometrical shapes and intuitive underlying physics along with substantially limited performance due to reduced internal degrees of freedom. The second approach finds the solution to the inverse problems by determining the material distribution, which ensures the desired optimal performance of the photonic device. The inverse algorithms lead to devices with nontrivial shapes and topologies, enabling high performance and compatibility with the predefined fabrication precisions. Inverse design optimization frameworks have been applied to traditional optimization problems in photonics, such as optimizing silicon photonic circuitry elements, 14–16 photonic crystal-based structures, 17 and metasurfaces. 18–20 Recently, topology optimization 21,22

Received: July 15, 2021 Published: October 1, 2021





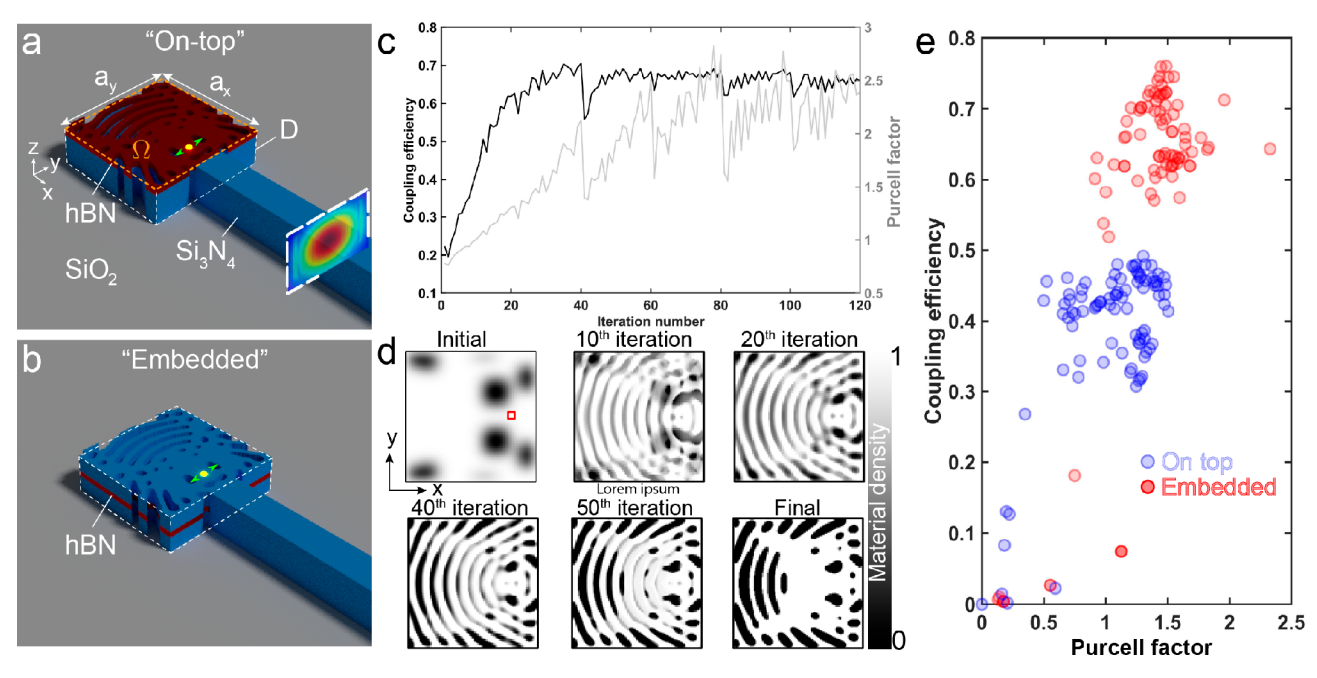


Figure 1. Topology optimization of the Si<sub>3</sub>N<sub>4</sub>-hBN hybrid coupler cavity. (a,b) Schematics of the optimization domain D for the (a) "on-top" and (b) "embedded" configurations of the Si<sub>3</sub>N<sub>4</sub>-hBN hybrid cavity on a SiO<sub>2</sub> substrate. The lateral cross-section  $\Omega$  of D with an area of  $a_x \times a_y$  ( $a_x = 2 \mu m$ ,  $a_y = 2 \mu m$ ) is highlighted by the dashed orange box in panel a. The total thickness of the optimized cavity is 200 nm, with a 50 nm thick hBN layer and a 150 nm thick Si<sub>3</sub>N<sub>4</sub> layer. SPS is assumed to be a point dipole source with its vector electric dipole moment aligned along the y axis and emitting at a wavelength of 638 nm. The position and orientation of the dipole moment are shown with the yellow marker. (c) Evolution of the coupling efficiency (black) and the Purcell factor (gray) during a TO run. (d) Corresponding evolution of the material density distribution inside the optimization area. The position of the SPS is shown with the red marker. The waveguide is assumed to be on the right side of the optimization area. (e) Distribution of the efficiencies versus the Purcell factor for each of the designs for the "on-top" (blue) and "embedded" (red) configurations.

(TO) was applied to various inverse design problems for quantum photonic applications. Namely, TO has been applied to realize efficient and coherent light-matter interfaces via the integration of nitrogen-vacancy- (NV) and tin-vacancy-centerbased single-photon sources (SPSs) within the diamond material platform.<sup>23</sup> TO has been used to control the emission of near-surface NVs in diamond with optimized silicon.<sup>24</sup> A related inverse design approach was applied to NV centers formed by implantation, where the surrounding gallium phosphide layer topology was optimized to enhance the photon extraction efficiency into free space radiation.<sup>25</sup> Within this work, we optimize the single-photon emission coupling efficiency of a point defect in a hexagonal boron nitride (hBN) flake into a predefined fundamental mode of the silicon nitride (Si<sub>3</sub>N<sub>4</sub>) waveguide. Specifically, we apply an adjoint TO framework to optimize the SPS coupler to enable (i) highefficiency emission coupling into the Si<sub>3</sub>N<sub>4</sub> waveguide and (ii) robustness of the design against perturbations introduced by the fabrication and uncertainty of the emitter position inside the hBN flake. Finally, we implement dimensionality reduction analysis on the TO designs, intending to gain insight into the physics behind the complex geometrical structures that leads to high-efficiency coupling. We demonstrate that such a rigorous analysis of the topology-optimized sets generates the initial material distribution, equivalent to an "educated guess" obtained with physics-driven human intuition. The proposed approach, which could take one from the "human-sketched" concept to the "computer-perfected" design of high-efficiency SPS couplers substantially faster, can be extended to other inverse design problems in photonics.

## ■ EFFICIENT CONVERSION OF SPS EMISSION VIA TOPOLOGY OPTIMIZED COUPLER

One of the possible ways of coupling SPSs into an on-chip infrastructure is to use evanescent coupling.<sup>26</sup> Recently, it has been demonstrated that placing an hBN flake with a color center on top of an aluminum nitride waveguide provides up to 1.2% extraction efficiency through the grating out-coupler.<sup>2</sup> Such a limited performance results from the low hBNwaveguide coupling efficiency (15.5%, numerical analysis) and grating out-coupler extraction efficiency (9.8%, measurements). The deterministic integration of SPSs in hBN into Si<sub>3</sub>N<sub>4</sub> waveguides has also been demonstrated.<sup>28</sup> It has been theoretically predicted that such an approach could yield ~20% coupling efficiency. Because the performance of such a hybrid system could be substantially improved by utilizing an inverse design optimization framework, we apply adjoint TO to design a high-efficiency coupler for an hBN-based SPS and a Si<sub>3</sub>N<sub>4</sub> waveguide. Specifically, we develop an inverse-designed Si<sub>3</sub>N<sub>4</sub>-hBN hybrid coupler that provides the high-efficiency conversion of SPS emission into the fundamental transverse magnetic (TM) mode of a 500  $\times$  200 nm<sup>2</sup> Si<sub>3</sub>N<sub>4</sub> waveguide placed on an SiO2 substrate.

In the developed quantum coupler design (Figure 1a), the optimization domain is a  $2 \times 2 \mu m^2$  cross-section area made of  $Si_3N_4$  and hBN layers with identical topologies. The SPS is assumed to be a point dipole source embedded inside the hBN layer, with its electric dipole moment aligned along the y axis and emitting at a wavelength of 638 nm (the zero-phonon line of color centers in hBN). Two different configurations are considered: "on-top", in which a 50 nm thick hBN is placed on top of the 150 nm thick  $Si_3N_4$  layer (Figure 1a), and

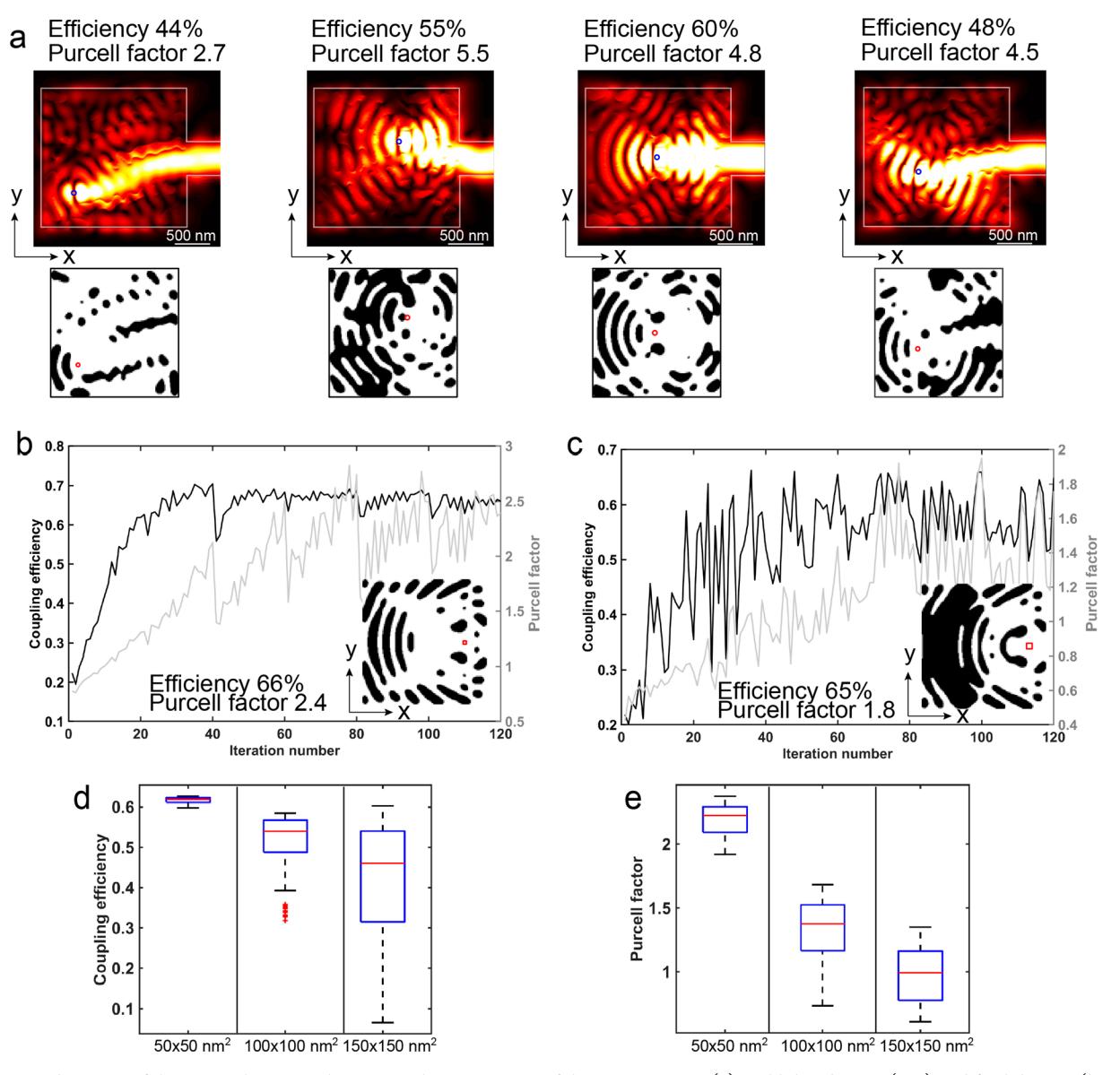


Figure 2. Robustness of the  $Si_3N_4$ -hBN coupler against the uncertainty of the SPE position. (a) Field distribution (top) and final designs (bottom) of the coupler for the off-center position. The position of the dipole source is highlighted by a red marker. (b,c) Convergence plots of the TO with the maximin decision rule for the robustness against uncertainty of the point defect position within a (b)  $50 \times 50$  nm² and (c)  $100 \times 100$  nm² area. Black curve: FoM; gray curve: Purcell factor. The insets show the final design of the  $Si_3N_4$ -hBN coupler. (d) Coupling efficiency and (e) Purcell factor distributions compared for the designs optimized with the maximin decision rule for the robustness against perturbations over the areas of  $50 \times 50$ ,  $100 \times 100$ , and  $150 \times 150$  nm². The boxed plot shows the median (red line), interquartile range (box), and outliers (red markers).

"embedded", in which the hBN slab is embedded between two 75 nm thick  $Si_3N_4$  layers (Figure 1b). One of the lateral sides of the optimization domain is connected to the  $Si_3N_4$  waveguide, and the propagation direction is assumed to be along the x axis.

The figure of merit (FoM) of the coupler is defined as the ratio between the fraction of the power emitted by the dipole source into the fundamental TEM mode and the total power emitted by the SPS, which is also denoted here as the coupling efficiency. Here we used an adjoint variation of the TO algorithm with sensitivity analysis, which enables the robustness control of optimized designs against the lateral perturbations of the SPS position introduced due to limited fabrication precision. <sup>29,30</sup>

The adjoint TO is realized via two full-wave simulations per optimization iteration, forward and adjoint, and employs a

commercial finite-difference time domain (FDTD) solver (Lumerical FDTD). The forward simulation is performed with dipole source excitation within the coupler domain D connected to the waveguide. In contrast, the adjoint simulation is conducted via the TM mode excitation in the backward direction. The dipole source (forward simulation) and the spatial distribution of the TM mode excitation used for the adjoint run are shown in Figure 1a. E-field distributions within D retrieved from forward and adjoint runs are then used to calculate the FoM gradient distribution in D. The FoM gradient values are used to update the material density distributions in the xy cross-section  $\Omega$  for the next iteration. More details of the adjoint TO framework can be found in the Supporting Information, Section S3. The choice of the initial material distribution plays an essential role in the adjoint TO framework. Initially, the material distribution in the opti-

mization domain is set to be a random, smooth distribution with the following permittivity function

$$\varepsilon(x, y) = \varepsilon_{\text{air}}[1 - \rho(x, y)] + \varepsilon_{\text{mat}}\rho(x, y), \quad \rho \in [0, 1]$$
(1)

where  $\rho(x,y)$  is the material density distribution that varies from 0 (air) to 1 (material) and  $\varepsilon_{\rm air}$  and  $\varepsilon_{\rm mat}$  are the dielectric constants of the air and material domains (Si<sub>3</sub>N<sub>4</sub> and hBN), respectively. The material distribution along the z axis is a uniform translation of the cross-section map, and the corresponding permittivity values are used within the Si<sub>3</sub>N<sub>4</sub> and hBN layers.

Figure 1c shows the convergence dynamics for one of the TO runs, depicting the evolution of the coupling efficiency during the optimization run. The coupling efficiency gradually increases and saturates around a steady-state local solution determined by the initial material distribution and parameters of the TO, such as parameters of the binary push and filtering procedures. (See the Supporting Information, Section S3.) The spikes in the FoM convergence plot are caused by the filtering algorithm suppressing subprecision features.

The optimization starts with a randomly selected initial material distribution and gradually converges to a binary material pattern at the very end of the optimization cycle (Figure 1d). We intentionally constrain material distribution around the dipole source position to a material density of the SiN/hBN to eliminate voids around the dipole. (See the highlighted red box in Figure 1d.)

Along with the coupling efficiency of the SPS into the waveguide, the Purcell factor, which defines the rate of the SPS's spontaneous emission, plays an important role. Previously, it has been demonstrated that the Purcell factor can be substantially increased via placing the SPS in a suitable photonic/plasmonic environment with an increased electromagnetic local density of states; <sup>32,33</sup> however, in this work, the TO is used for optimization of the coupling efficiency. The Purcell factor optimization can also be explicitly incorporated into the TO framework. During the TO process, along with the increase in the coupling efficiency, a ~2.5-fold increase in the Purcell factor of the structure is achieved (Figure 1c, gray curve). Such an increase in the Purcell factor is mainly driven by the rise in the quality factor of the Si<sub>3</sub>N<sub>4</sub>-hBN coupler. Such a moderate increase is the result of the constrained uniform material distribution around the dipole source. By unconstrained optimization of the coupler design, it is possible to substantially increase the Purcell factor (~15-fold) while maintaining a high coupling efficiency. However, such an approach might lead to impractical coupler designs containing air voids around the dipole position and need additional postselection of the optimized structures. On the basis of the developed TO framework, we conducted 85 optimization runs for each of the "on-top" and "embedded" geometrical configurations (Figure 1e). The "embedded" configuration provides more efficient coupler designs in terms of both the coupling efficiencies (76%) and the Purcell factor (2.5), whereas the best design in the "on-top" set yields only 49% coupling efficiency and a 1.5-fold Purcell factor (Figure 1e).

# OFF-CENTER CONFIGURATION AND ROBUSTNESS

In the previous section, the TO is realized for a fixed position of the SPS dipoles; however, in reality, it is challenging to realize. Moreover, because of the limited precision of the localization of point defects in hBN flakes, the coupler designs should be robust against the uncertainty of the SPS position within the  $Si_3N_4$ -hBN coupler.

In this section, we showcase the off-center configuration of the coupler and incorporate the robustness procedure into the TO algorithm against perturbations due to imperfect SPS positioning. For the off-center configuration, the position of the dipole is randomly picked within the optimization domain. Specifically, we consider four different positions of the dipole (red markers, Figure 2a). Corresponding field distributions and resulting coupler designs are also shown in Figure 2a. Here we consider "embedded" designs configurations for all off-center cases. The field distributions prove that optimized cavities indeed enable higher efficiency conversion of the emission into the waveguide mode. From the coupler designs, it can be seen that the TO leads to the formation of "Bragg-grating"-type material distribution around the SPS, which leads to more efficient redirection of the field toward the waveguide. The offcenter position of the SPS leads to a reduction of the coupling efficiency (<55%) while providing relatively high values of the Purcell factor (Figure 2a). Such reduction of the coupling efficiency occurs due to a relatively small refractive index of Si<sub>3</sub>N<sub>4</sub>. One possible way of overcoming this issue is to increase the dimensions of the Si<sub>3</sub>N<sub>4</sub>-hBN coupler, which would allow the redirection of the SPS emission into the waveguide adiabatically. On the contrary, the same simulation examples show that off-center cases provide a relatively large Purcell factor. Such enhancement of the Purcell factor depends on the material distribution around the SPS source. Within the considered off-center cases, the Purcell factor increases due to the formation of air voids around the SPS due to the formation of a dielectric cavity with a high quality factor. Yet another vital aspect is the robustness of Si<sub>3</sub>N<sub>4</sub>-hBN couplers against the uncertainty in the point defect position within the hBN layer. Such uncertainty occurs due to the limited precision of the SPSs' positioning within the hBN flake. To include such a constraint, we implemented a maximin decision rule into the TO framework. (See the Supporting Information, Section S3). For each TO iteration, the dipole source was placed into randomly chosen positions within a predefined area. Corresponding FoMs were assessed by conducting forward simulation runs. The configuration with the lowest FoM value was used to determine the material gradient distribution, and the material distribution was updated for the next iteration. Such a maximin technique allows for convergence to a coupler design that is robust against the uncertainty of the positioning of the SPS within the predefined area (Figure 2b). Along with the evolution of the FoM, the Purcell factor also evolves along the TO run (Figure 2b), which eventually yields a robust cavity with 66% coupling efficiency and a 2.4 Purcell factor for the case of a  $50 \times 50 \text{ nm}^2$  optimization area.

We also studied the convergence of the FoM and the Purcell factor for the case of SPS position perturbation within the  $100 \times 100 \text{ nm}^2$  area (Figure 2c). In this case, the TO ensures 65% coupling efficiency and a 1.8 Purcell factor. One should note that the larger perturbation areas of the SPS position perturbation lead to unstable convergence of the TO. Both cases were realized via probing three different SPS positions at each iteration. Hence each TO iteration is realized via four fullwave runs in total (three forward runs and one adjoint FDTD run). To test the performance of the final devices, we optimized three structures with a maximin decision rule applied to  $50 \times 50$ ,  $100 \times 100$ , and  $150 \times 150 \text{ nm}^2$  areas. The

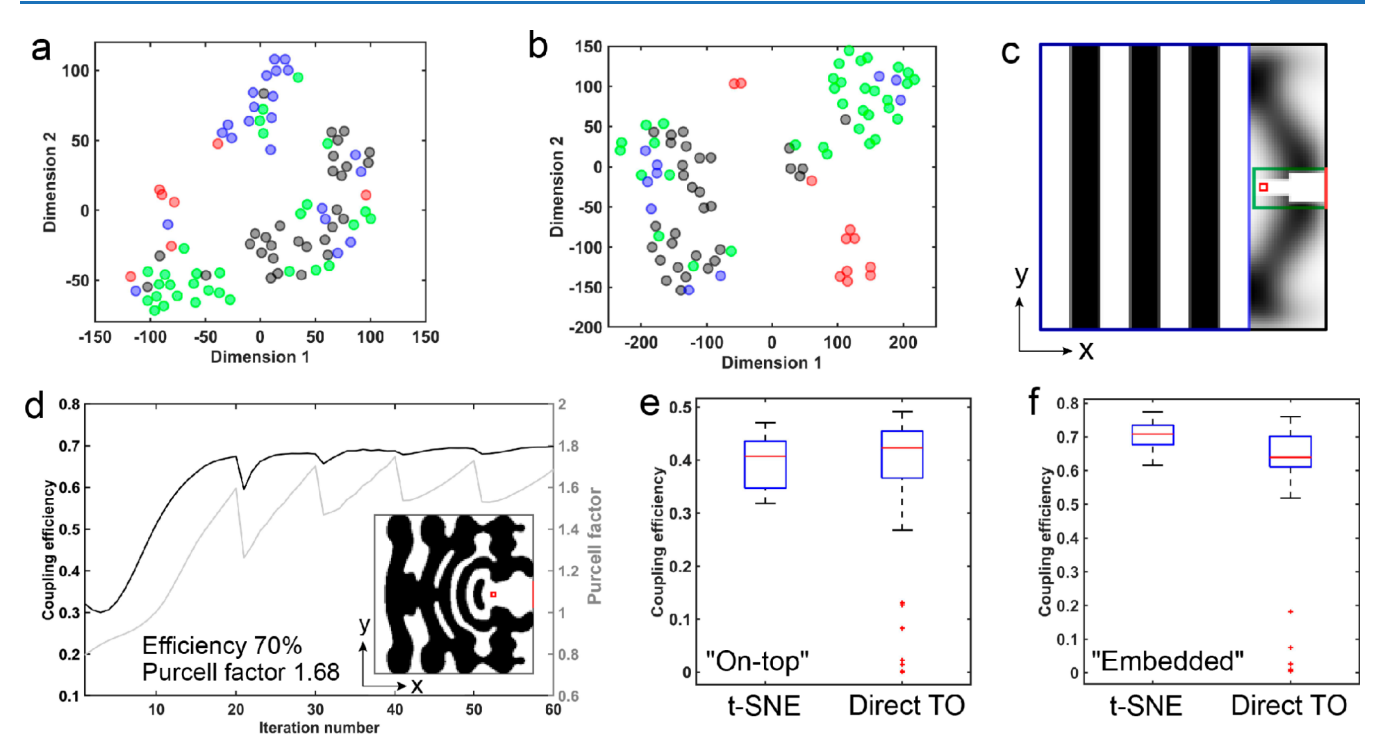


Figure 3. Dimensionality reduction analysis. (a,b) Dimensionality-reduced design distributions obtained via t-SNE for (a) "on-top" and (b) "embedded" configurations. For the "on-top" configuration, the classes are defined as: class 1: efficiency <10% (red markers), class 2: efficiency between 10 and 35% (blue), class 3: efficiency between 35 and 40% (green), and class 4: efficiency >40% (black). For the "embedded" configuration, these classes are defined as: class 1: efficiency <10% (red markers), class 2: efficiency between 10 and 55% (blue), class 3: efficiency between 55 and 65% (green), and class 4: efficiency >65% (black). (c) Initial material distribution obtained via t-SNE analysis. Blue highlight: A Bragg-reflector-like structure behind the emitter position; green highlight: Si<sub>3</sub>N<sub>4</sub> distribution within the area connecting the position of the emitter and the waveguide; red square: position of the dipole source, surrounded by a constant material density of 1. (d) Convergence plots of the TO with the initial conditions shown in panel c. Black curve: FoM; gray curve: Purcell factor. Insets show the final design of the Si<sub>3</sub>N<sub>4</sub>-hBN coupler. (e,f) Convergence plots of the TO with initial material distributions chosen based on the design rule derived from t-SNE analysis ("t-SNE") and random initial conditions ("Direct TO") for the (e) "on-top" and (f) "embedded" configurations. The box plot shows the median (red line), interquartile range (box), and outliers (red markers).

position of the source dipole was swept in 10 nm steps along both lateral directions in the preselected areas of the optimized devices, and the corresponding coupling efficiencies and Purcell factors were retrieved. The statistics of the coupling efficiency and the Purcell factors are shown in Figure 2d,e, respectively. The TO with a maximin decision rule applied for the  $50 \times 50 \text{ nm}^2$  area ensures highly robust performance of the device with a median FoM at 61.8% and an interquartile range (25th to 75th percentile) between 61 and 62.2%. For comparison, the  $100 \times 100 \text{ nm}^2$  robustness case has a median at 54% and an interquartile range between 48.8 and 56.8%, whereas the  $150 \times 150 \text{ nm}^2$  case has the median at 46% and an interquartile range between 31.5 and 54%. The Purcell factor distributions show the same behavior. Whereas the  $50 \times 50$ nm<sup>2</sup> area case shows a narrow distribution of the Purcell factor (median at 2.22 and interquartile range between 2.09 and 2.29), the 100  $\times$  100 and 150  $\times$  150 nm<sup>2</sup> cases exhibit distributions with medians at 1.37 and 1, respectively. From this analysis, we conclude that the  $50 \times 50 \text{ nm}^2$  area case shows the most robust performance of the coupler with a deviation of the coupling efficiency within 1.2%. The 100  $\times$ 100 nm<sup>2</sup> ensures quite good stability of coupling efficiency (deviation within 8%), whereas perturbation of the dipole source position within  $150 \times 150 \text{ nm}^2$  leads to the unstable performance of the designed Si<sub>3</sub>N<sub>4</sub>-hBN coupler.

#### DIMENSIONALITY REDUCTION ANALYSIS

A commonly used strategy with an adjoint TO framework is executing the same optimization algorithm with different initial conditions many times and picking the most efficient solution within the obtained set; however, this approach leads to an apparent trade-off between the time/resources and the target performance. Such a dilemma arises because randomly selected initial conditions might lead to low-efficiency designs at the end of the time-consuming optimization run. Thus there is a critical need to build a comprehensive understanding of what essential geometrical features should be initially included to increase the success rate of the TO. To build such an intuition, we applied a dimensionality reduction technique to the optimized design data sets and analyzed a clustering of the high-efficiency TO designs based on their geometrical features. Specifically, we apply t-distributed stochastic neighbor embedding (t-SNE), which is well suited for embedding high-dimensional data for visualization in 2D/3D-dimensional spaces.<sup>34</sup> This method allows us to represent each TO design by a 2D point and form clusters of such points representing designs with similar geometrical features. By analyzing the correlation between such clusters and the corresponding design efficiencies, it is possible to gain insight into the critical geometrical features of the coupler design that lead to increased performance.

We use coupler design patterns as high-dimensional data; the corresponding coupling efficiencies are used as labels. To

make the t-SNE analysis more meaningful, we grouped all of the TO designs into four main classes based on the design's coupling efficiency by the k-means clustering method. This method partitions all of the classes into a reasonable number of clusters in which each label belongs to the cluster with the nearest mean (centroids).<sup>35</sup>

After assigning a class to each design, we employed the t-SNE algorithm and obtained dimensionality-reduced distributions for "on-top" (Figure 3a) and "embedded" (Figure 3b) configurations of the coupler. We found that all of the designs group into four clusters based on their geometrical similarity. It is important that this clustering has a good correlation with assigned efficiency classes, which indicates a connection between the efficiency of the coupler and its shape/topology. The efficiency classes are denoted with different marker colors. The classes are assigned based on the efficiency of the coupler. A visual and simple statistical analysis is applied to t-SNE plots to develop design rules for future optimizations. We formulate the design rules as two essential procedures: (i) enforcing material distributions in the selected locations and (ii) providing intuitive initial material density distributions (Figure 3c). The first constrain restricts the material distribution in certain areas to remain intact throughout the optimization. These regions include (a) the proximity of the SPS (red square, Figure 3c,d) and (b) the cross-section connecting the SPS and the waveguide (red segment, Figure 3c,d). The details of this analysis, along with the application of the machinelearning algorithms, are presented in the Supporting Information, Section S4.

On the basis of this analysis, we conclude that two regions of the initial material distributions play the critical role: (1) a Bragg-reflector-like structure behind the emitter position (blue highlight, Figure 3c) and (2) the Si<sub>3</sub>N<sub>4</sub> distribution within the area connecting the position of the emitter and the waveguide (green highlight, Figure 3c). Figure 3c shows an example of the initial material distribution used for TO. The TO-related evolution of the coupling efficiency and the convergence of the Purcell factor yield 70% and 1.68 values, respectively (Figure 3d). We found that the initial condition of Figure 3c, chosen by the design rules and obtained from the t-SNE analysis, enables fast and stable convergence to highly efficient coupler designs (Figure 3d). To prove this point, we conducted 25 TO runs for "on-top" and "embedded" configurations. Figure 3e,f compares the coupling efficiencies of designs obtained from TO with either t-SNE-based or random-sampling-based initial conditions. It is no surprise that the initial conditions are indeed similar to the structures already proposed in the literature for integrated SPSs with Bragg reflectors and tapered waveguide cross sections.<sup>3,36</sup> This provides an excellent route to speed-up and ensure robust convergence through a physicsdriven initial geometry fed into the TO framework. We note that such an initial "educated guess" could be done classically without the t-SNE and then perfected via TO.

We found that in the case of the "on-top" coupler, the t-SNE case has a much narrower efficiency distribution, whereas the maximum efficiency is slightly less (47%) than that in the case of direct TO (49%) with random sampling. The median of the t-SNE case distribution is 41% versus the direct TO-produced distribution with a 42% median value. In the "embedded" case, the t-SNE-based initial condition gives a much better coupling efficiency distribution (71% median and 78% maximum efficiencies) versus the direct TO, which ensures only 64% median and 76% maximum efficiencies. Hence the t-SNE-

based analysis indeed leads to a better convergence of the TO algorithm.

#### CONCLUSIONS

The main high-efficiency components of QPICs, such as SPE couplers, linear and nonlinear photonic components for quantum-state manipulation, and out-couplers, are the focus of intensive research due to their importance in the realization of novel quantum information processing applications. Along with efficiency, compatibility with the fabrication precision of state-of-the-art fabrication technology is one of the main constraints for the design and development process. In this work, we developed an optimization framework to design efficient structures to couple the emission from a point defect in 2D materials, specifically, hBN, acting as a single photon emitter SPS to a photonic waveguide using adjoint topology optimization. The proposed TO method provides significantly enhanced coupling efficiency and drastically improved Purcell factors. We optimized the couplers for two different material configurations and created a library of designs to gain deeper insights into the optimal device's performance.

We also demonstrated that physics-informed, intuitive initial conditions ensure rapid and robust optimization and produce high-performance devices that could pave the way to practical realizations of room-temperature SPSs. Our approach enables fast and robust convergence with a physics-driven "educated guess"—an initial material distribution that could be obtained without the t-SNE but perfected with the TO. Overall, the highest performing device achieves a coupling efficiency of 78% with a nearly two times enhanced Purcell factor. As the next steps, fabrication imperfections and color center location uncertainties should be studied, and the experimental realization of devices should be explored. The developed design approach can be extended to coupling schemes utilizing different SPSs and other inverse design problems in photonics.

#### ASSOCIATED CONTENT

### **Solution** Supporting Information

The Supporting Information is available free of charge at https://pubs.acs.org/doi/10.1021/acsphotonics.1c01070.

Additional details of the adjoint topology optimization of on-chip SPS, step-by-step explanation of the optimization procedure, details of the "Dimensionality Reduction Analysis", and the design rules derivation (PDF)

Field evolution versus time in an optimized coupler (MP4)

#### AUTHOR INFORMATION

#### **Corresponding Author**

Alexander V. Kildishev — School of Electrical and Computer Engineering, Birck Nanotechnology Center and Purdue Quantum Science and Engineering Institute, Purdue University, West Lafayette, Indiana 47907, United States; orcid.org/0000-0002-8382-8422; Email: kildishev@purdue.edu

#### **Authors**

Omer Yesilyurt — School of Electrical and Computer Engineering, Birck Nanotechnology Center and Purdue Quantum Science and Engineering Institute, Purdue University, West Lafayette, Indiana 47907, United States;

- The Quantum Science Center (QSC), a National Quantum Information Science Research Center of the U.S. Department of Energy (DOE), Oak Ridge, Tennessee 37931, United States; occid.org/0000-0002-9829-5219
- Zhaxylyk A. Kudyshev School of Electrical and Computer Engineering, Birck Nanotechnology Center and Purdue Quantum Science and Engineering Institute, Purdue University, West Lafayette, Indiana 47907, United States; The Quantum Science Center (QSC), a National Quantum Information Science Research Center of the U.S. Department of Energy (DOE), Oak Ridge, Tennessee 37931, United States; orcid.org/0000-0002-6955-0890
- Alexandra Boltasseva School of Electrical and Computer Engineering, Birck Nanotechnology Center and Purdue Quantum Science and Engineering Institute, Purdue University, West Lafayette, Indiana 47907, United States; The Quantum Science Center (QSC), a National Quantum Information Science Research Center of the U.S. Department of Energy (DOE), Oak Ridge, Tennessee 37931, United States; orcid.org/0000-0001-8905-2605
- Vladimir M. Shalaev School of Electrical and Computer Engineering, Birck Nanotechnology Center and Purdue Quantum Science and Engineering Institute, Purdue University, West Lafayette, Indiana 47907, United States; The Quantum Science Center (QSC), a National Quantum Information Science Research Center of the U.S. Department of Energy (DOE), Oak Ridge, Tennessee 37931, United States

Complete contact information is available at: https://pubs.acs.org/10.1021/acsphotonics.1c01070

#### **Author Contributions**

<sup>§</sup>O.Y. and Z.A.K. contributed equally.

#### Notes

The authors declare no competing financial interest.

#### ACKNOWLEDGMENTS

This work is supported by the U.S. Department of Energy (DOE), Office of Science through the Quantum Science Center (QSC), a National Quantum Information Science Research Center (developing ML algorithms), the DARPA/DSO Extreme Optics and Imaging (EXTREME) Program (HR00111720032) (O.Y., A.V.K., Z.A.K., TO techniques), and National Science Foundation award 2029553-ECCS.

### **■** REFERENCES

- (1) O'Brien, J. L.; Furusawa, A.; Vučković, J. Photonic Quantum Technologies. *Nat. Photonics* **2009**, 3 (12), 687.
- (2) Kim, J.-H.; Aghaeimeibodi, S.; Carolan, J.; Englund, D.; Waks, E. Hybrid Integration Methods for On-Chip Quantum Photonics. *Optica* **2020**, *7* (4), 291.
- (3) Lukin, D. M.; Guidry, M. A.; Vučković, J Integrated Quantum Photonics with Silicon Carbide: Challenges and Prospects. *PRX Quantum* **2020**, *1* (2), 020102.
- (4) Thomas, S. E.; Billard, M.; Coste, N.; Wein, S. C.; Priya; Ollivier, H.; Krebs, O.; Tazairt, L.; Harouri, A.; Lemaitre, A.; Sagnes, I.; Anton, C.; Lanco, L.; Somaschi, N.; Loredo, J. C.; Senellart, P. Bright Polarized Single-Photon Source Based on a Linear Dipole. *Phys. Rev. Lett.* 2021, 126 (23), 233601.
- (5) Wan, N. H.; Lu, T.-J.; Chen, K. C.; Walsh, M. P.; Trusheim, M. E.; de Santis, L.; Bersin, E. A.; Harris, I. B.; Mouradian, S. L.; Christen, I. R.; Bielejec, E. S.; Englund, D. Large-Scale Integration of Artificial Atoms in Hybrid Photonic Circuits. *Nature* **2020**, 583 (7815), 226.

- (6) Weber, J. R.; Koehl, W. F.; Varley, J. B.; Janotti, A.; Buckley, B. B.; van de Walle, C. G.; Awschalom, D. D. Quantum Computing with Defects. *Proc. Natl. Acad. Sci. U. S. A.* **2010**, *107* (19), 8513–8518.
- (7) Northup, T. E.; Blatt, R. Quantum Information Transfer Using Photons. *Nat. Photonics* **2014**, *8* (5), 356.
- (8) Gisin, N.; Ribordy, G.; Tittel, W.; Zbinden, H. Quantum Cryptography. Rev. Mod. Phys. 2002, 74 (1), 145.
- (9) Polyakov, S. v.; Migdall, A. L. High Accuracy Verification of a Correlated-Photon-Based Method for Determining Photoncounting Detection Efficiency. *Opt. Express* **2007**, *15* (4), 1390.
- (10) Kupko, T.; von Helversen, M.; Rickert, L.; Schulze, J.-H.; Strittmatter, A.; Gschrey, M.; Rodt, S.; Reitzenstein, S.; Heindel, T. Tools for the Performance Optimization of Single-Photon Quantum Key Distribution. *npj Quantum Information* **2020**, *6* (1), 29.
- (11) Steinbrecher, G. R.; Olson, J. P.; Englund, D.; Carolan, J. Quantum Optical Neural Networks. *npj Quantum Information* **2019**, 5 (1), 60.
- (12) Wang, J.; Sciarrino, F.; Laing, A.; Thompson, M. G. Integrated Photonic Quantum Technologies. *Nat. Photonics* **2020**, *14* (5), 273.
- (13) Molesky, S.; Lin, Z.; Piggott, A. Y.; Jin, W.; Vucković, J.; Rodriguez, A. W. Inverse Design in Nanophotonics. *Nat. Photonics* **2018**, *12* (11), 659.
- (14) Wang, K.; Ren, X.; Chang, W.; Lu, L.; Liu, D.; Zhang, M. Inverse Design of Digital Nanophotonic Devices Using the Adjoint Method. *Photonics Res.* **2020**, *8* (4), 528.
- (15) Piggott, A. Y.; Ma, E. Y.; Su, L.; Ahn, G. H.; Sapra, N. v.; Vercruysse, D.; Netherton, A. M.; Khope, A. S. P.; Bowers, J. E.; Vučković, J. Inverse-Designed Photonics for Semiconductor Foundries. *ACS Photonics* **2020**, *7* (3), 569.
- (16) Hughes, T. W.; Minkov, M.; Williamson, I. A. D.; Fan, S. Adjoint Method and Inverse Design for Nonlinear Nanophotonic Devices. *ACS Photonics* **2018**, 5 (12), 4781.
- (17) Minkov, M.; Williamson, I. A. D.; Andreani, L. C.; Gerace, D.; Lou, B.; Song, A. Y.; Hughes, T. W.; Fan, S. Inverse Design of Photonic Crystals through Automatic Differentiation. *ACS Photonics* **2020**, *7* (7), 1729.
- (18) Liu, Z.; Zhu, D.; Rodrigues, S. P.; Lee, K.-T.; Cai, W. Generative Model for the Inverse Design of Metasurfaces. *Nano Lett.* **2018**, *18* (10), 6570.
- (19) Kudyshev, Z. A.; Kildishev, A. v.; Shalaev, V. M.; Boltasseva, A. Machine-Learning-Assisted Metasurface Design for High-Efficiency Thermal Emitter Optimization. *Appl. Phys. Rev.* **2020**, *7* (2), 021407.
- (20) Kudyshev, Z. A.; Kildishev, A. v.; Shalaev, V. M.; Boltasseva, A. Machine Learning—Assisted Global Optimization of Photonic Devices. *Nanophotonics* **2020**, *10* (1), 371.
- (21) Bendsøe, M. P.; Sigmund, O. *Topology Optimization*; Springer Berlin Heidelberg: Berlin, 2004. DOI: 10.1007/978-3-662-05086-6.
- (22) Jensen, J. S.; Sigmund, O. Topology Optimization for Nanophtonics. *Laser & Photonics Reviews* **2011**, 5 (2), 308.
- (23) Rugar, A. E.; Aghaeimeibodi, S.; Riedel, D.; Dory, C.; Lu, H.; McQuade, P. J.; Shen, Z.-X.; Melosh, N. A.; Vučković, J. A Quantum Photonic Interface for Tin-Vacancy Centers in Diamond. *Phys. Rev. X* **2021**, *11*, 031021.
- (24) Wambold, R. A.; Yu, Z.; Xiao, Y.; Bachman, B.; Jaffe, G.; Kolkowitz, S.; Choy, J. T.; Eriksson, M. A.; Hamers, R. J.; Kats, M. A. Adjoint-Optimized Nanoscale Light Extractor for Nitrogen-Vacancy Centers in Diamond. *Nanophotonics* **2020**, *10* (1), 393.
- (25) Chakravarthi, S.; Chao, P.; Pederson, C.; Molesky, S.; Ivanov, A.; Hestroffer, K.; Hatami, F.; Rodriguez, A. W.; Fu, K.-M. C. Inverse-Designed Photon Extractors for Optically Addressable Defect Qubits. *Optica* **2020**, *7* (12), 1805.
- (26) Mnaymneh, K.; Dalacu, D.; McKee, J.; Lapointe, J.; Haffouz, S.; Weber, J. F.; Northeast, D. B.; Poole, P. J.; Aers, G. C.; Williams, R. L. On-Chip Integration of Single Photon Sources via Evanescent Coupling of Tapered Nanowires to SiN Waveguides. *Advanced Quantum Technologies* **2020**, 3 (2), 1900021.
- (27) Kim, S.; Duong, N. M. H.; Nguyen, M.; Lu, T.; Kianinia, M.; Mendelson, N.; Solntsev, A.; Bradac, C.; Englund, D. R.;

Aharonovich, I. Integrated on Chip Platform with Quantum Emitters in Layered Materials. *Adv. Opt. Mater.* **2019**, 7 (23), 1901132.

- (28) Elshaari, A. W.; Skalli, A.; Gyger, S.; Nurizzo, M.; Schweickert, L.; Esmaeil Zadeh, I.; Svedendahl, M.; Steinhauer, S.; Zwiller, V. Deterministic Integration of HBN Emitter in Silicon Nitride Photonic Waveguide. Advanced Quantum Technologies 2021. Adv. Quantum Tech. 2021, 4, 2100032.
- (29) Lalau-Keraly, C. M.; Bhargava, S.; Miller, O. D.; Yablonovitch, E. Adjoint Shape Optimization Applied to Electromagnetic Design. *Opt. Express* **2013**, *21* (18), 21693.
- (30) Sell, D.; Yang, J.; Doshay, S.; Yang, R.; Fan, J. A. Large-Angle, Multifunctional Metagratings Based on Freeform Multimode Geometries. *Nano Lett.* **2017**, *17* (6), 3752.
- (31) Christiansen, R. E.; Sigmund, O. Inverse Design in Photonics by Topology Optimization: Tutorial. *J. Opt. Soc. Am. B* **2021**, *38* (2), 496.
- (32) Bogdanov, S. I.; Shalaginov, M. Y.; Lagutchev, A. S.; Chiang, C.-C.; Shah, D.; Baburin, A. S.; Ryzhikov, I. A.; Rodionov, I. A.; Kildishev, A. v.; Boltasseva, A.; Shalaev, V. M. Ultrabright Room-Temperature Sub-Nanosecond Emission from Single Nitrogen-Vacancy Centers Coupled to Nanopatch Antennas. *Nano Lett.* **2018**, *18* (8), 4837.
- (33) Bogdanov, S. I.; Boltasseva, A.; Shalaev, V. M. Overcoming Quantum Decoherence with Plasmonics. *Science* **2019**, *364* (6440), 532.
- (34) van der Maaten, L.; Hinton, G. Visualizing Data Using t-SNE. *J. Mach. Learn. Res.* **2008**, *9*, 2579–2605.
- (35) MacQueen, J. Some Methods for Classification and Analysis of Multivariate Observations. *Proceedings of the Fifth Berkeley Symposium on Mathematical Statistics and Probability* **1967**, *5.1*, 281–297.
- (36) Kim, S.; Fröch, J. E.; Christian, J.; Straw, M.; Bishop, J.; Totonjian, D.; Watanabe, K.; Taniguchi, T.; Toth, M.; Aharonovich, I. Photonic Crystal Cavities from Hexagonal Boron Nitride. *Nat. Commun.* **2018**, 9 (1), 2623.